Mapping Ice Buried by the 1875 and 1961 Tephra of Askja Volcano, Northern Iceland using Ground-Penetrating Radar: Implications for Askja Caldera as a Geophysical Testbed for In-Situ Resource Utilization

E. S. Shoemaker[1*†], D. M. H. Baker[2], J. A. Richardson[2], L. M. Carter[1], S. P. Scheidt[2,3], P. L. Whelley[2,3], and K. E. Young[2]

[1]Lunar and Planetary Laboratory, University of Arizona, Tucson, AZ, 85721, [2]NASA Goddard Space Flight Center, Greenbelt, MD, 20771, [3]University of Maryland, College Park, MD, 20742.

*Corresponding author: Emileigh Shoemaker (emileigh.s.shoemaker@nasa.gov)

[†]Now at NASA Goddard Space Flight Center, Greenbelt, MD, 20771

Key Points:

- Multi-frequency GPR surveys identified massive ice up to 4.4 m thick buried by up to 1 m of tephra from two Holocene eruptions of Askja
- GPR readily maps vertical and horizontal extents of subsurface ice and tephra overburden; ice concentration transitions are not detected
- Ice-rich and ice-free sites present a similar attenuation; ice-rich sites demonstrate lower attenuation rate with increasing ice thickness

Abstract

Eruptions of the Askja Volcano in Northern Iceland in 1875 and 1961 blanketed the caldera with rhyolitic and basaltic tephra deposits, respectively, which preserved layers of seasonal snowpack as massive ice. Askja serves as an operational and geophysical analog to test ground-penetrating radar field and analysis techniques for *in-situ* resource utilization objectives relevant to the martian and lunar environments. We conducted ground-penetrating radar surveys at center frequencies of 200, 400, and 900 MHz to map the thickness and extent of tephra deposits and underlying massive ice at three caldera sites. We identified up to 1 meter of tephra preserving up to 4.5 meters of massive ice. We measured the real dielectric permittivity of the overlying tephra and the total attenuation at each frequency of the tephra and ice. A key objective of our investigation was to determine if this attenuation (or loss) could be used as an additional, identifying characteristic of massive ice preserved at depth when compared to ice-free stratigraphy. Loss rates of the ice-rich subsurface decreases with increasing ice thickness relative to the overburden which may constitute a possible signature. Attenuation also increased with increasing frequency. The tephra, ice, and other volcanic deposits at each of our three caldera sites and the ice-free pumice-mantled 1961 Vikrahraun lava flow exhibited a characteristically low loss rate at all frequencies. This result highlights the ambiguity associated with identifying the unique signature of ice within low-loss stratigraphies, a possible challenge for its identification in the martian or lunar subsurface using radar.

Plain Language Summary

The Askja Volcano in Northern Iceland is considered to be a planetary analog for other terrestrial worlds like Mars and the Moon. We conducted ground-penetrating radar surveys of the Askja caldera where seasonal snowpack was buried by eruptions of low-density ash and tephra in 1875

and 1961. This erupted volcanic material protected the snowpack long-term where it later densified into thick layers of ice. We successfully mapped up to 4.5 m of this ice preserved beneath up to 1 m of erupted material. Transmitted radar signals decay naturally as their distance from the source increases. Some materials such as water ice are less conducting than others and are therefore less lossy to this transmitted signal. We used the ice and tephra deposits at Askja as a test case to determine if large quantities of buried ice would result in a detectable signature that indicates its presence when compared to ice-free regions. We found that increases in ice layer thickness relative to the overlying volcanic material results in columns of material with bulk properties that are less dissipative to the radar signal and therefore may indicate a signature of buried ice in the subsurface.

1 Introduction

Ground-penetrating radar (GPR) instrumentation is widely employed in periglacial and glacial settings on Earth to characterize the subsurface physical properties of ice, soil, and sediment in the upper 10s to 100s of meters of the subsurface. GPR has been identified as a non-invasive and easily deployable tool to investigate the subsurface and characteristics of regolith and ice-containing sites on the Moon and Mars (e.g., Grimm et al., 2006; Heggy et al., 2006a; 2006b; Boisson et al., 2011; MEPAG ICE-SAG Report, 2019; Lai et al., 2019; LWIMS Report, 2020; Hamran et al., 2020; Li et al., 2020; Richardson et al., 2020; Hamran et al., 2022; Li et al., 2022; Shoemaker et al., 2022 and references therein). Orbital radar sounders were the first systems used to identify and confirm widespread, buried ice deposits across the midlatitudes of Mars (e.g., Picardi et al., 2004; Seu et al., 2007; Holt et al., 2008; Bramson et al., 2015;

Stuurman et al., 2016; Dundas et al., 2018; Morgan et al., 2021). GPR systems have now been successfully deployed on rovers on the surfaces of Mars and the Moon (Fang et al., 2014; Hamran et al., 2020; 2021; Li et al., 2020; Li et al., 2022). There is significant interest in including a GPR system as part of a future *in-situ* resource utilization (ISRU) campaign to a polar cold trap on the Moon, similar in scope to the upcoming VIPER mission (Volatiles Investigating Polar Exploration Rover) (LWIMS Report, 2020; Colaprete, 2021; Shoemaker et al., 2022).

Terrestrial analog field sites are critical to test GPR methods to successfully characterize the properties of subsurface regolith and ice for future ISRU campaigns (Dinwiddie et al., 2005; Grimm et al., 2006; Heggy et al., 2006a; 2006b; Brandt et al., 2007; Boisson et al., 2011; Campbell et al., 2018). At an elevation of >1 km, Askja is in a region of discontinuous permafrost (Etzelmüller et al., 2007; Czekirda et al., 2019; Etzelmüller et al., 2020) that has been uniquely influenced by its regional volcanic activity and historical deposits of tephra (Kellerer-Pirklbauer et al., 2007). Askja provides a geophysical testbed to probe shallow (0-10 m) ice deposits similar in thickness and burial to those on Mars or potentially the Moon. Analytical and field deployment methods can be readily developed there to achieve future science and ISRU objectives for terrestrial bodies (Cannon and Britt, 2020; Ellery, 2020; Starr and Muscatello, 2020). A current challenge in utilizing GPR for coordinated resource campaigns are the ambiguous results it can yield of subsurface stratigraphy. This has been demonstrated for layers such as water ice and a low-density regolith, which share similar dielectric properties (Boisson et al., 2011). Different depositional processes may also share similar morphologies in radar returns ("radar facies"), which can complicate interpretations that guide real-time science objectives of *in-situ* surface missions (e.g., Hamran et al., 2022). Our investigation seeks to determine if the total losses to the radar signal can be used as an additional, diagnostic signature of the presence of subsurface water ice when compared to ice-free locations, given several meters of buried ice at Askja. To accomplish this, we conducted the first multi-frequency GPR mapping campaign to characterize the thickness, extent, and dielectric properties of the massive ice and pyroclastic deposits at the Askja Volcano located in the Northern Icelandic Highlands (Figure 1a).

2 Askja Eruptions and Caldera Site Description

The Askja central volcano is located in the Northern Volcanic Zone (NVZ) of Iceland (Figure 1a, inset). Askja was the source of a series of recent explosive and effusive eruptions in 1875, 1921-1922, 1929, 1931 and 1961 in addition to many other, earlier Holocene eruptions (Annertz, Nilsson, and Sigvaldason 1985; Carey et al., 2008a; 2008b; Graettinger et al., 2013; Hartley et al., 2016). The youngest and current caldera is Öskjuvatn (Figure 1a), now occupied by a lake, formed by an explosive phreatoplinian eruption in March 1875 (Sparks et al., 1981; Carey et al., 2009; Carey et al., 2010; Graettinger et al., 2013). The March 1875 eruption produced 0.33 km^3 dense rock equivalent (DRE) of tephra throughout eastern Iceland and parts of Scandinavia and Germany (Carey et al., 2009). The caldera tephra deposit is a coarse, sub-angular, rhyolitic pumice (referred to as Unit D; Sparks et al., 1981) along with an underlying unit of gray/brown massive ash fall and/or intracaldera pyroclastic surge deposits (broadly referred to as Unit C; Sparks et al. 1981; Carey et al., 2010). In October-

November 1961, vents near the northern rim of the caldera deposited a black-brown, basaltic lapilli and some ash throughout the caldera and the Vikrahraun lava flow was emplaced eastward from the rim (Thorarinsson & Sigvaldason, 1962; Blasizzo et al., 2022). These two tephra deposits each blanketed and preserved a layer of seasonal snowpack that later densified into massive ice (an extensive layer comprised mostly of lithic-poor ice) (Helgason, 2000; Carey et al., 2009). This permafrost aggradation process initiated via snowpack burial and preservation by volcanic tephra has been observed elsewhere in Iceland in its early stages at the Hekla volcano after its 2000 eruption and possibly in its much later stages at Öræfajökull preserved by ash from its eruption in 1362 (Helgason 2000; Kellerer-Pirklbauer et al., 2007). Various thermokarst and permafrost landforms are observed across the Askja caldera and flanks that indicate the presence of ice at depth.

We focus on three sites within the caldera that are blanketed by these tephra deposits (Figure 1b, white boxes). We chose these sites because they possess morphologic evidence that buried ice is present and represent the major tephra deposits and near-surface stratigraphy observed within this region of the caldera. Figure 1c-e show each of these three sites and associated GPR surveys taken in 2019 and 2021 (yellow lines). From north to south, Site 1 (Figures 1c and 2a) possesses massive ice buried by the 1961 tephra deposit, Site 2 (Figures 1d and 2b) captures the 1961 tephra beginning to transition to the 1875 tephra, and Site 3 (Figures 1e and 2c) is primarily blanketed by the 1875 tephra with 1961 tephra mostly confined to topographic depressions. These three sites exhibit a range of tephra overburden types and clast sizes, ice thickness, and permafrost landforms, making this region of Askja an excellent site to test GPR field and data analysis techniques.

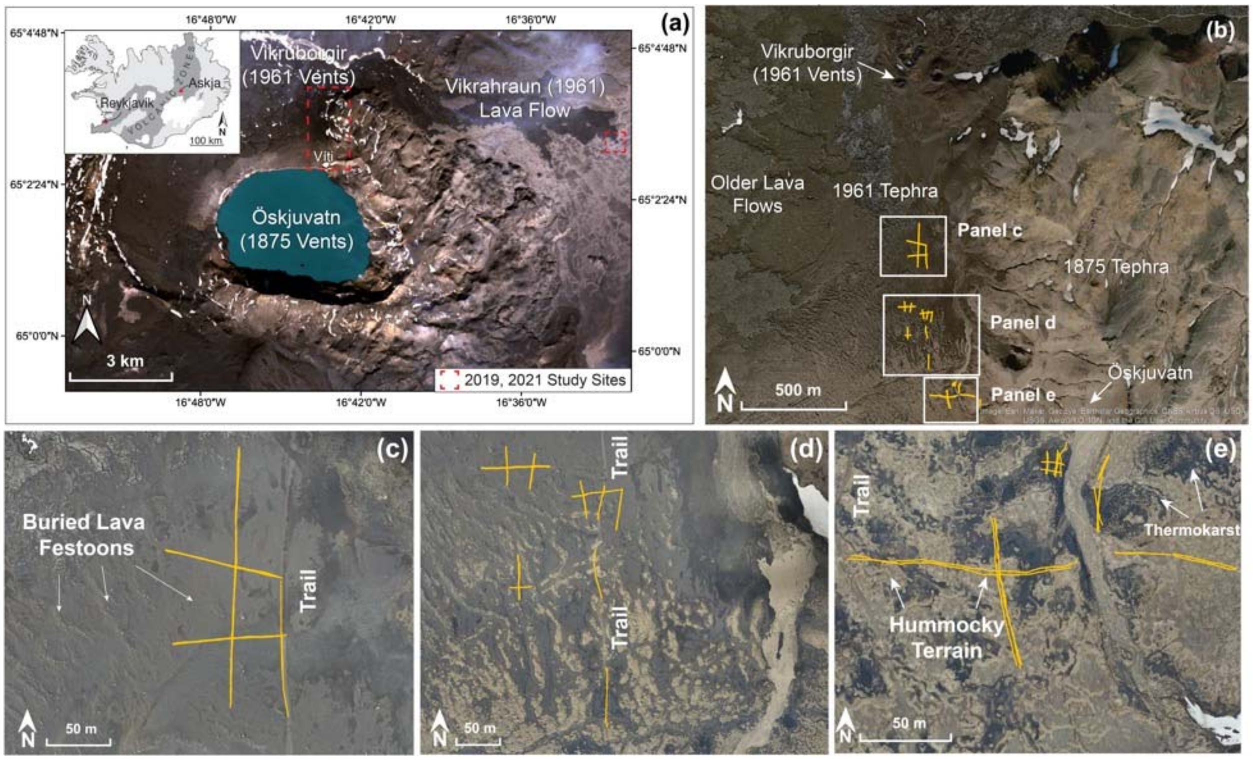

Figure 1. Askja is a central volcano located in Northern Iceland (panel a inset). (a) Deposits of buff-colored rhyolitic pumice and black/brown basaltic tephra from eruptions in 1875 and 1961, respectively, cover the northeastern part of the caldera. These deposits preserve ice at depth. Ground-penetrating radar (GPR) surveys were conducted within the caldera and at the toe of the 1961 Vikrahraun lava flow (red boxes). **(b)** Within the caldera, GPR surveys were concentrated in two main regions: within the 1961 tephra deposit to the north (panel c) and a zone where 1961 tephra transitions to 1875 pumice (panels d, e). **(c, d, e)** Sites 1, 2, and 3, respectively, where GPR data were collected at 200, 400, and 900 MHz in summer 2019 and 2021. GPR traverses at all center frequencies taken in 2019 and 2021 are collectively shown in yellow. Panel (a) basemap is Landsat-8 pansharpened image LC8_217015_20140906 (Vermote et al., 2016). Panel (b) basemap obtained from the Esri ArcGIS™ software.

3 Methods

3.1 Field Methods

We conducted two GPR field campaigns within the Askja caldera in July-August 2019 and in August 2021 on rain-free days. At each site during both campaigns, relatively dry conditions and porous tephra kept moisture levels in the subsurface to a minimum, except at the ice table where small amounts of perched meltwater were observed. We used a Geophysical Survey Systems Inc. (GSSI) SIR 4000 GPR system with three shielded antennas operating at center frequencies of 200, 400, and 900 MHz for surveys. Cross-sectional images of the subsurface (radargrams) were collected as a series of individual traces along the length of a traverse across the surface. Traces were collected in distance mode by an attached odometer wheel where the profile of the subsurface was sampled at 100 traces/meter. Radargrams are displayed as two-way travel times (or depth) of returned radar wave amplitudes as a function of along-traverse distance (Figure 3). Strong contrasts in dielectric constant, or the real relative permittivity (proportional to density), between subsurface materials will appear as a distinct, bright boundary, or reflector, at depth. These reflections allowed us to map the horizontal and vertical extent of tephra and ice layers across the Askja caldera.

Position and altitude of the GPR unit was controlled using a combination of differential GPS (dGPS) and contextual high-resolution aerial surveys of the caldera floor using a small uncrewed aerial system (UAS) DJI Mavic Pro. Traverses were georegistered and terrain-corrected using a Trimble Geo7x Handheld GPS attached to the GPR unit with a tens-of-centimeter-to-meter position accuracy. UAS surveys took place in 2019 and 2021 to provide detailed knowledge of surface lithology, water and ice, terrain height, and additional positional control of GPR transects. UAS images were used to produce orthomosaics (Figure 1c-e) and corresponding digital elevation models of our survey sites. The 2019 mosaic and elevation model data products were produced at a spatial resolution < 3 cm/pixel in AgiSoft Metashape software; 2021 data products were produced at < 6 cm/pixel. UAS data products were georegistered to a horizontal and vertical precision < 5 cm/pixel with a post-processing kinematic (PPK) dGPS survey conducted at stationary markers laid out in the UAS Survey area. Additionally, we drilled boreholes and dug trenches along collected GPR traverses to collect observations of tephra stratigraphy variations across the caldera and to verify subsurface reflectors identified in radargrams, locate the top of the ice table at survey sites, and note changes in moisture conditions with depth.

3.2 Quantifying Permittivity and EM Wave Velocity

The permittivity of geologic materials is an intrinsic property expressed as a complex number: $\varepsilon^* = \varepsilon' - i\varepsilon''$. The ratio of the imaginary component, ε'', describing signal losses, and the real component, ε', is the loss tangent, $tan\delta$. This quantity is, in turn, related to the attenuation of the radar signal (see Section 3.4). Relative permittivity is given by $\varepsilon_r = \varepsilon/\varepsilon_0$ where ε_0 is the permittivity of free space. The real component of the relative permittivity, ε_r', (or dielectric constant; hereafter “permittivity” for brevity) is related to the radar wave propagation through a medium which is given by

$$v = c/\sqrt{\varepsilon_r'} \qquad (1)$$

where v is the bulk velocity of the radar wave through the medium and c is the speed of light in vacuum. ε_r' of subsurface layers was estimated at different sites using two methods. First, we estimated the velocity and calculated permittivity (Eq. 1) from trench measurements of tephra thickness and the one-way travel times from radar picks at the tephra-ice interface. Second, we estimated bulk velocity by fitting theoretical hyperbolas to hyperbolic forms that are generated by the motion of the GPR system toward, over, and away from an embedded subsurface scatterer. We use the GSSI RADAN 7 processing and analysis software to fit hyperbolas where possible and report estimates of bulk velocity and permittivity for those sections of the subsurface above the embedded point sources.

3.3 Mapping Ice and Tephra Thicknesses

We produced maps of ice and tephra thickness at each site by picking radar reflectors within collected radargrams. We applied a time-zero correction and an exponential gain to the radargrams prior to picking. This gain was applied only for visualization purposes and removed for any calculations. We used the open source Radar Analysis Graphical Utility (RAGU) picking software (Tober and Christoffersen, 2020) to generate our reflector inventory. From each picked reflector, we exported relevant quantities to an ESRI shapefile, including radar amplitudes, latitude and longitude, two-way travel times, elevation, and layer thickness. Layer thicknesses were calculated using permittivity values estimated using the two methods described in Section 3.2, with a trench or borehole measurement preferred if available. Each shapefile was then input into GIS software where it was overlaid onto the caldera orthoimages. Examples of these ice thickness maps are shown in Figures 2 and S1.

3.4 Quantifying Losses to the Radar Signal

Total losses to the radar signal are sourced from intrinsic attenuation (i.e., absorption), scattering, and the geometric spreading of the transmitted wave front as it travels through the subsurface and back to the receiver. Losses are directly proportional to distance, R, and exhibit a semilogarithmic decay in amplitude with depth (or travel time) given by $e^{-2\alpha R}$, for uniform layer thicknesses and constant reflection coefficients, where α is the attenuation coefficient (Grimm et al., 2006). This behavior can also arise from an isotropic distribution of scatterers (Grimm et al., 2006). Similar behavior has been observed in seismology (e.g., Jin et al., 1994; Farrokhi et al., 2016) and in both cases, this constant decay is referred to as Q where $Q^{-1} = tan\delta = \alpha\lambda/\pi$, where tan δ is loss tangent and λ is the wavelength. To quantify the losses to the radar signal, we employ methods similar to Grimm et al. (2006) and Boisson et al. (2011) and fit sections of averaged amplitudes that exhibit a semilogarithmic decay with depth. To estimate the total loss and Q from the amplitudes at each GPR antenna frequency, we first applied a series of processing steps to the GPR data, including (in order): 1) time-zero correction, 2) horizontal background filter to remove sources of coherent backscatter, 3) Hilbert transform to obtain the magnitude of collected traces and to further reduce signal variation, and 4) amplitude-normalization using the peak of the direct wave. From the processed data, we then calculated the average of traces over a segment of the radargram where layers were constant in time-delay and maintained uniform thickness.

Total attenuation is estimated from trace averages corrected for ground losses such as the geometric spreading of the wavefront and the backscatter cross sections of the reflecting targets. These losses are described by the radar equation (Annan & Davis, 1977; Skolnik, 2008), the ratio of the reflected power to the transmitted power:

$$\frac{P_R}{P_T} = \frac{G^2\lambda^2\xi}{64\pi^3R^4}e^{-4\alpha R} \qquad (2)$$

where G is antenna gain, λ is the radar wavelength, ξ is the backscatter cross-section, α is the intrinsic attenuation coefficient, and R is the distance to the reflecting target. After correcting the relative amplitudes for these effects, total attenuation can be isolated from the average trace (Annan & Davis, 1977; Boisson et al., 2011; Grimm et al., 2006; Scabbia & Heggy, 2018).

Three models are considered for the backscatter cross-section, ξ: 1) a smooth, planar reflector where $\xi = \pi R^2\Gamma$ where Γ is the power reflection coefficient, therefore, $P_R/P_T \propto 1/R^2$, 2) GPR returns are integrated over the diameter of the first Fresnel zone $(\sqrt{2}\lambda R)$ (e.g., a rough, planar reflector) and $\xi = \pi\lambda R\Gamma/2$ yielding $P_R/P_T \propto 1/R^3$, and 3) a collection of Rayleigh scatterers, or subwavelength-sized spheres, yielding $\xi = \pi^5 D^6\Gamma/\lambda$ where D is the radius of the sphere yielding $P_R/P_T \propto 1/R^4$ (Annan & Davis, 1977).

We applied all three models to correct the trace averages, however, the rough reflector and Rayleigh scatterer models overcorrected the data, which generated an unrealistic, positive slope. We therefore applied a model-dependent gain function of the form $1/R^2$ to the average trace, where R is depth in meters. Round-trip travel times are converted to depth using a three-layer permittivity model. Permittivity of the overlying tephra is fairly well constrained from trenches and at the base of that layer (see Sections 3.2 and 4.2). We assume a permittivity of 3.2 for ice at temperatures at or around 0ºC for microwave frequencies (Johari et al., 1976; Matsuoka et al., 1997). Our assumption of the permittivity of the deepest layer then depends on our observations at each site, further discussed in Section 4.3 (see Table S3 for layer permittivity). One-way loss rates in dB/m are estimated from linear least-squares fits to the portion of the corrected average trace exhibiting an exponential decay with depth, from the position of the first positive peak of the corrected average trace to the noise floor (see Figure 4a-d). We used the slope from our fits to estimate loss tangent where $tan\delta^{-1}$ = Q. We used this total attenuation to test whether the presence of massive ice at depth would result in a lower loss when compared to ice-free stratigraphy.

Estimates of losses, Q , and loss tangent were made using open-source Python code developed by Shoemaker (2023).This code depends on the open-source Python software readgssi (Nesbitt et al., 2022) and functions from the open-source Python software RAGU (Tober and Christoffersen, 2020) to read in and auto-detect the peak of the direct wave from each collected GSSI radargram prior to averaging traces, correcting the total loss curve for spreading and scattering effects, and fitting.

4 Results

4.1 Distribution of Ice and Tephra at Surveyed Sites

We examined 57 radargrams collected across the three caldera sites at central frequencies of 200, 400, and 900 MHz (Figure 1). Dominant tephra layers at Sites 1-3 are the 1961 tephra and 1875 tephra Units C and D (Sparks et al. 1981; Carey et al., 2010). Unit D is a Plinian fall deposit of well-sorted lapilli. We observed some larger cm-to-dm-sized pumice clasts at Site 3. Unit D thicknesses of up to 200 cm proximal to Öskjuvatn are estimated by Carey et al. (2010). Unit C underlies D and is a gray/brown massive ash fall up to ~20-25 cm thick in Site 3 and potentially present at Sites 1 and 2 at depth. Intracaldera pyroclastic surge deposits comprise subunits of C but are confined to regions proximal to Öskjuvatn and not present at our sites of interest.

Reflections associated with the top of subsurface massive ice (and base of the tephra layer(s)) were identified in GPR data at each of the sites. We summarize maximum tephra and massive ice thicknesses for all sites estimated at 400 MHz in Table 1.

Table 1. Estimates of massive ice thickness and tephra overburden thickness from 400 MHz GPR observations for the three caldera sites.

Site	Tephra Cover	Maximum Tephra Thickness (m)	Maximum Massive Ice Thickness (m)
1	1961 Basaltic Tephra	~1.5	2.8
2	1961 Basaltic Tephra	~0.8	4.4
3	1875 Tephra	~2.0	2.8

Corresponding ice thickness estimates for each of the three sites at 400 MHz (for clarity) are shown in Figure 2. A summary of ice thickness for the collected radargrams at each site and at all frequencies can be found in Figure S1 in the Supporting Information. Ice thickness could not be estimated for all GPR traverses. In limited cases, it was difficult to identify the ice layer at depth due to scattering in the capping tephra layer or poor coupling to the surface by the antenna. We excluded 900 MHz data at Site 3 from ice estimates because of this. In other cases, the lower resolution at 200 MHz prevented identification of thin layers of tephra. A discussion of observations at individual sites follows this section.

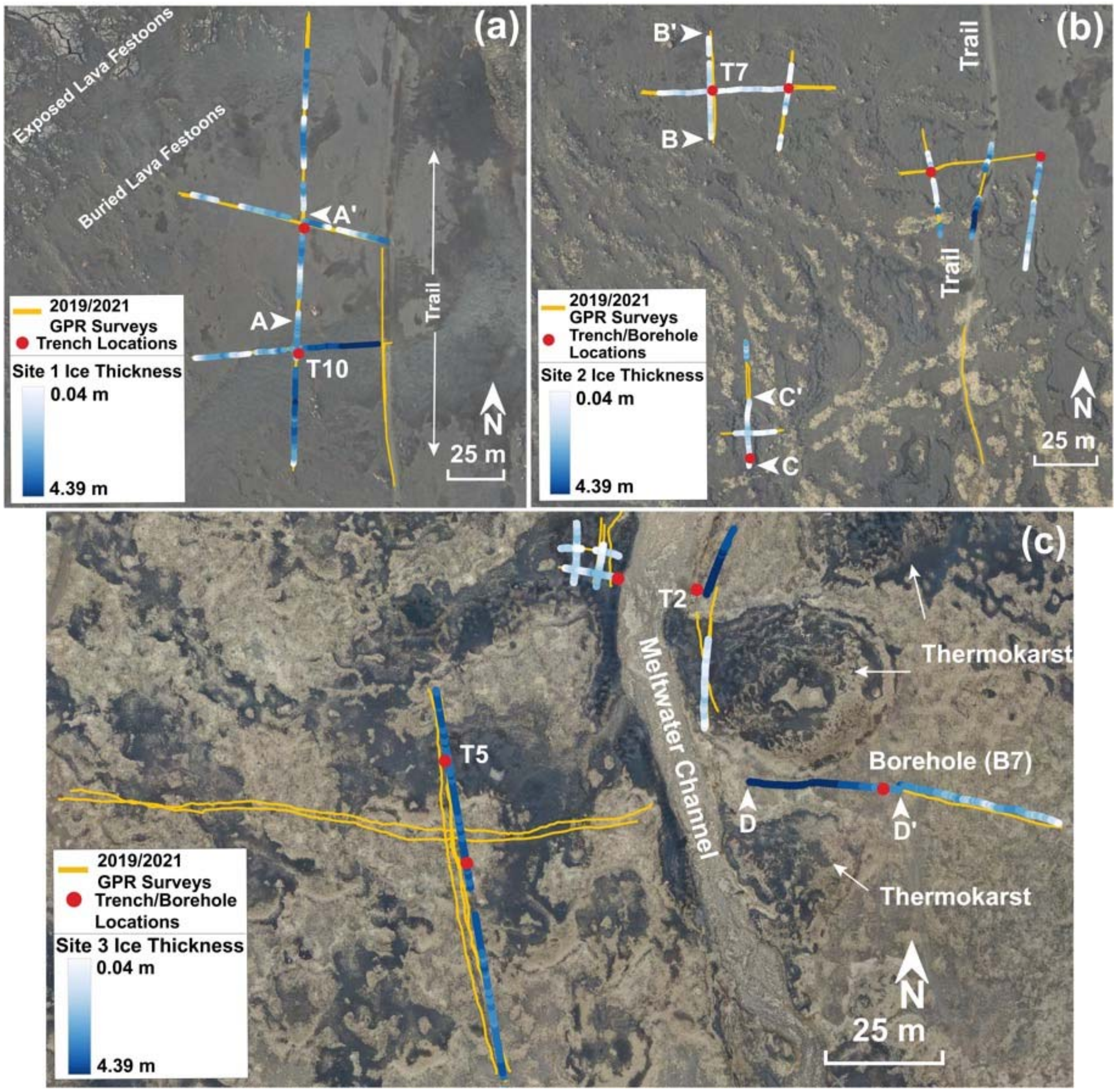

Figure 2. We mapped massive ice buried by tephra using ground-penetrating radar at center frequencies of 200, 400, and 900 MHz. Panels a, b, and c are ice thickness maps summarized for the 400 MHz observations. Massive ice was observed to be thickest at Site 2, panel (b), reaching depths of 4.39 m. Radargrams collected at each center frequency at each of the three sites are summarized in Figure 3. Trench and borehole locations are marked in red. **(a)** Site 1 massive ice deposits are thinner in the west and thicken toward the hiking trail in the east, reaching a maximum depth of 2.79 m. The tephra transitions from more loosely packed ripples or aeolian bedforms to a smoother, compact section after point A. Internal layering was observed within the less compact tephra. **(b)** Site 2 has more ablation features than Site 1 (e.g., tension cracks and depressions). Massive ice here is likely resting on an older ash or tephra deposited prior to 1961. Massive ice deposits are also thickest at this site, reaching a maximum of 4.39 m moving south along the hiking trail. **(c)** Massive ice at Site 3 tends to be thicker, on average, beneath the 1875 pumice. Obvious thermokarst are scattered throughout this region. A meltwater channel generated by seasonal melting of snow cuts through GPR traverses taken

on either side. Trenches taken on the east and west banks of this channel revealed ice buried by tephra from the 1875 and 1961 eruptions. Images of the interplay of these deposits and massive ice along with labeled trenches and boreholes from this figure are shown in Figure 4.

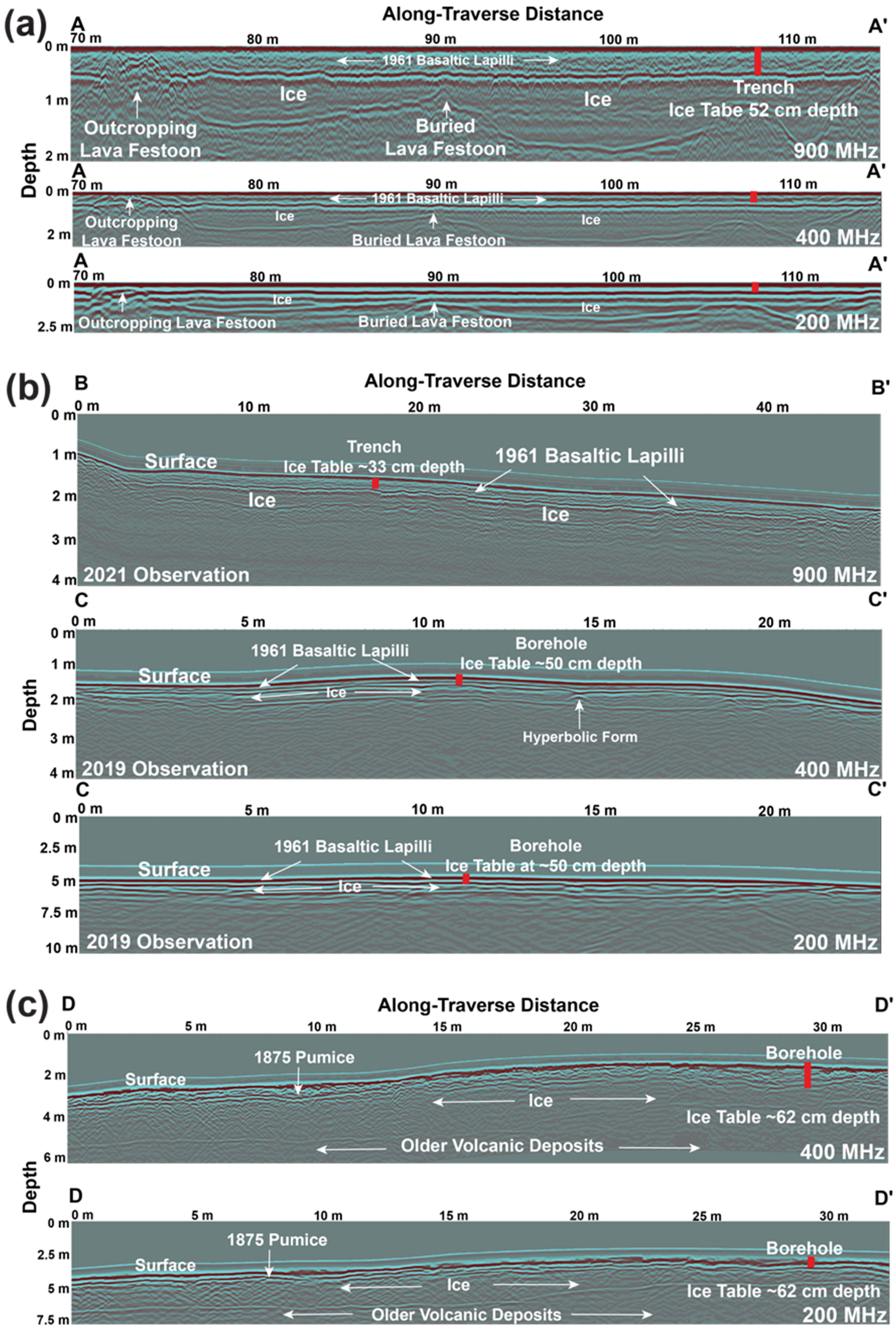
(a)
A
A'
Along-Traverse Distance
70 m
80 m
90 m
100 m
110 m
0 m
1 m
2 m
Depth
1961 Basaltic Lapilli
Ice
Ice
Trench
Ice Tabe 52 cm depth
Outcropping
Lava Festoon
Buried
Lava Festoon
900 MHz
400 MHz
200 MHz
2.5 m
Outcropping Lava Festoon
Buried Lava Festoon
(b)
B
B'
0 m
10 m
20 m
30 m
40 m
3 m
4 m
Surface
Trench
Ice Table ~33 cm depth
1961 Basaltic Lapilli
2021 Observation
C
C'
5 m
15 m
Borehole
Ice Table ~50 cm depth
Hyperbolic Form
2019 Observation
7.5 m
10 m
Ice Table at ~50 cm depth
(c)
D
D'
25 m
1875 Pumice
Ice Table ~62 cm depth
Older Volcanic Deposits
6 m

Figure 3. (a) Site 1 radargrams correspond to panel (a) of Figure 2. A section of a 206 m traverse is shown from A to A' where up to ~2 m of massive ice occupies the troughs of buried lava flow festoons. The top of the ice table is fairly constant, measured from trenching to be at 52 cm depth beneath the 1961 tephra. From the ice table position, an average permittivity of 2.91 is applied to place the ice table at its observed depth in the images. **(b)** Site 2 radargrams correspond to panel (b) of Figure 2. Section B to B’ is a 900 MHz observation with relatively thin ice (~50 cm) preserved by ~33 cm of 1961 tephra taken in 2021. This radargram was depth-corrected using a derived tephra permittivity of 7. Section C to C' is repeat 400 and 200 MHz observations taken in 2019 where up to 65 cm of massive ice is preserved by ~50 cm of 1961 tephra. These radargrams were depth-corrected using a permittivity of 2.59. **(c)** Site 3 radargrams correspond to panel (c) of Figure 2. Radargrams from D to D' were taken upslope. The cm-to-dm-sized clasts of pumice from 1875 are visibly more scattering than the sub-wavelength 1961 tephra. Massive ice reaches a maximum thickness for Site 3 along this section at 2.84 m. The ice table is estimated to be at ~62 cm from a borehole 29 m along-traverse. These radargrams were depth-corrected using an average tephra permittivity of 4.59. All radargrams were processed in the GSSI RADAN 7 software using a vertical infinite impulse response (IIR) filter, a five-point exponential gain, and corrected for variations in surface topography.

Figure 4. Trenches and boreholes were taken along various GPR traverses at each of the three sites in the caldera and on the 1961 Vikrahraun lava flow. Trench and borehole numbers correspond to labeled red points in Figure 2. Site 1 **(a)** and 2 **(b)** are blanketed by ~30-50 cm of black/brown basaltic lapilli mixed with some gray/brown ash from the 1961 eruption overlying massive ice. These trenches were dug to the top of the ice table in each case. 1875 tephra (Units C and D) are likely present below the ice table overlying other, older basalt lava flows (e.g., Carey et al., 2010) but were not observed in the trenches. Site 3 trenches in panels **(c)** and **(d)** show the interplay between black/brown 1961 tephra, massive ice, and the 1875 tephra deposits. In (c), ~15 cm black/brown lapilli and coarse ash from 1961 give way to 15 cm of moist brown ash with mm-to-cm-sized blocks of buff colored 1875 pumice. The ice table rests at 30 cm depth. T2 in (d) was dug on a slope of the eastern meltwater channel bank in Figure 2c, making observed depths larger than vertical. ~25 cm coarse, mm-to-cm-size clasts of black/brown 1961

tephra and gray/brown ash transitions to ~15 cm of pore ice and 70 cm of massive ice. ~53 cm of an ice-cemented, pumice-supported coarse-to-fine ash matrix from 1875 extends to the floor of the channel, which is comprised of a 50/50 mixture of pumice clasts and ice from 1875. **(e)** Borehole B7 (Figure 2c) was taken at 29 m along radargrams in Figure 3c. This retrieval (arranged in discontinuous but depth-ordered sections) shows the transition from ice-cemented 1875 pumice and ash to massive ice from bottom to top in the image. The ice table was measured to be at 62 cm depth.The trench was taken along the eastern meltwater channel bank near these GPR traverses. ~40 cm of cm-sized 1875 pumice with ash is burying ~3 m of massive ice at Site 3. **(f)** This trench was dug along the western bank of the meltwater channel at Site 3 where 36 cm of 1961 basaltic lapilli was covering ~60 cm of massive ice that was resting on moist, brown 1875 ash deposits with some mm-to-cm-sized clasts of buff colored 1875 pumice. **(g)** GPR traverses across the toe of the 1875 pumice-mantled 1961 Vikrahraun lava flow found ~1 m of pumice rests atop the basalt flow. 1875 tephra was finer-grained at this site (mm-sized grains and fine-grained ash). Stratigraphy is ice-free.

4.1.1 Site 1 Observations

Site 1 contains GPR observations primarily taken during the 2021 field season. The 1961 basaltic tephra is visible at the surface as black/brown lapilli with some gray/brown ash mixed in. A series of long traverses (up to 206 m) were repeated at 200, 400, and 900 MHz over the 1961 basaltic tephra deposit (Figures 1c, 2a, and 4a). From visual observations taken on the surface, this tephra deposit is uniform in physical properties such as appearance, grain size, porosity, and compaction along each survey line. Trenches were dug along the GPR traverse lines, with locations shown in Figure 2. At trench T10 (Figure 4a), the black/brown basaltic 1961 lapilli extends to the top of the ice table at ~40 cm depth. Isopach maps from Carey et al. (2010) indicate that 1875 Unit D and potentially C may be present at depth. We did not observe any tephras in the trenches at Site 1 that matched the descriptions of these units. It is therefore likely that if present, they were emplaced prior to snowpack that was later preserved by the 1961 tephra and are stratigraphically lower at this site.

Tephra in the southernmost portion of Site 1 is slightly finer-grained, having been remobilized to form ripples or aeolian bedforms. In radargrams, this area of ripples on the surface corresponds to a series of closely-spaced, shallow reflectors within the 1961 tephra deposit interpreted to result from internal layering and moisture differences. These reflectors are confined to regions with surface ripples at the start and end of the longest traverse in Figure 2a. The ice deposit is thickest (~1.4–2.8 m thick) in the south (beneath these bedforms) and east (toward the hiking trail). Indeed, the reflectors identified at the top and base of the massive ice deposit are seen to extend beneath these regions of surface ripples. The transition from these bedforms to a smoother, more compact tephra is visible in Figure 2a just before point A.

Massive ice layers at Site 1 are discontinuous in radargrams (Figure 3a), and are thickest in troughs within what is interpreted as an older, underlying lava flow. Ice pinches out toward structures interpreted to be buried lava festoons (arcuate surface ridges at m-to-tens-of-m spacing formed by increases in viscosity as lava cools while the interior continues to flow). Trenching revealed the ice table at fairly consistent depths between 40 and 52 cm, except where disrupted by lava festoons. Some lava festoons are exposed along the survey line (e.g., near point A) as rocky outcrops at the surface, where they also generated clutter in the GPR data. It may be that 1875 tephras (Units C and D) are present beneath the ice table and overlying these buried lava flows. We do not see multiple reflections associated with these units if they are present, they may be thin enough to be at the resolution limit of the radar antennas used. The mm-to-cm-sized clasts of lapilli generated little scattering visible in the radargrams, as compared to Site 3 (see Section 4.1.3) where most of the ice is buried by the cm-to-dm-sized 1875 pumice.

4.1.2 Site 2 Observations

1961 basaltic tephra covers the surface of Site 2 with some windblown 1875 pumice fragments scattered across the surface (Figures 1d and 2b). GPR surveys were taken across regions almost exclusively covered by 1961 tephra. Ablation and melt-related features are more widespread here than at Site 1, observed as collapsed depressions, tension cracks, and hummocks along with pooled surface water and some perched meltwater at the ice table. Many of these depressions appear to be concentrated or have initiated near the boundaries between subsurface ice and abutting lava outcrops. Surveys were taken along the trail and in a region west of the trail where melting has generated several "islands" of massive ice at depth that are surrounded by collapse features and small hummocks (Figure 2b, B to B').

Massive ice layers are fairly continuous in the radargrams (Figure 3b), but are disrupted by ablation and where collapse features are evident at the surface. The tephra cover is consistently thinner at this site, which could be the reason for the increase in ablation features compared to Site 1. Ice deposits are thicker in the east toward the hiking trail, approaching 5 m and are as thin as 9 cm in the western portions. The ice table was at depths of 33-50 cm in trenches, and is well resolved at each frequency. The massive ice layer in each radargram shows very little scattering or internal reflectors, implying low lithic content and/or dispersed, entrained sediment of small grain size. This is consistent with ice samples retrieved from boreholes and trenches at this site.

Trench T7 at Site 2 (Figure 4b) shows black/brown 1961 tephra present as lapilli down to the ice table at 33 cm with some gray/brown ash from the same eruption. The 1875 tephra

(Units C and D) are absent from the trenches at this site. The isopach maps from Carey et al. (2010) suggest these layers may be present below the ice table we observed. The radargrams in Figure 3b show a reflector at the base of the ice in all cases. It is likely this reflector is generated by the massive ice in contact with these 1875 tephra units. We do not resolve multiple reflectors at depth, however. Unit C is likely thinner than Unit D at this site and is therefore not resolved by the radar antennas we used.

4.1.3 Site 3 Observations

At Site 3, both 1961 and 1875 tephra layers and buried ice are observed, including large hummocks of 1875 tephra and depressions infilled by 1961 tephra bounded by tension cracks (Figure 1e and 2c). GPR traverses were primarily taken along the banks of a large, seasonal meltwater channel, which allowed easy access to vertical stratigraphy exposed though trenching. Trenches and boreholes from Site 3 are shown in Figure 4c-f.

A trench (Figure 4c) dug at point T5 along the southwest traverse captures 1961 lapilli overlying 1875 tephra and massive ice. 1875 tephra Units C and D are present in this layer. Figure 2c On the eastern bank of the channel, a trench revealed a transition from ~25 cm coarse, mm-to-cm-size clasts of black/brown lapilli and gray/brown ash from 1961 to ~15 cm of pore ice and 70 cm of massive ice. ~53 cm of an ice-cemented, pumice-supported coarse-to-fine ash matrix from 1875 extends to the floor of the channel (Units D and C). Another trench on the eastern bank ~3 m of massive ice was buried beneath ~40 cm of cm-sized 1875 tephra (Figure 4e). Pumice clasts in this image are from the 1875 Unit D (Carey et al., 2010). On the western channel bank within a large depression, ~60 cm of ice buried by 36 cm of black/brown 1961 basaltic lapilli was uncovered on top of 1875 ash and pumice (Figure 4f). Both ice deposits had little entrained sediment and closed, mm-sized gas bubbles/pore space.

Figure 3c shows radargrams from D to D' at Site 3 where up to 2.84 m of ice is buried exclusively by 62 cm of cm-to-dm-sized clasts of 1875 tephra and ash. A borehole retrieval shown in Figure 4e shows the transition from ice-cemented pumice clasts to massive ice. In contrast to the minimal scattering by the 1961 basaltic lapilli, the 1875 pumice layer shows strong scattering behavior in radargrams until it contacts the top of the ice table. A weaker basal interface is observed for the ice layer at both frequencies. The region between the ice table top and base is transparent in radargrams suggesting fairly uniform ice with little entrained sediment or bedding at wavelength-scale, which was confirmed by both trenches exposing massive ice along the channel banks and a borehole taken close to D' (see Figure 4d-f).

4.2 Permittivity and Wave Velocity

Velocity measurements within the 1875 tephra were more challenging than for the 1961 tephra. Scattering from 1875 pumice clasts approaching the wavelengths of the antennas generated many overlapping hyperbolic forms, especially at 400 and 900 MHz. Hyperbola fits were therefore scarce at Site 3 where the 1875 pumice is much more prevalent. We summarize all of the successful individual hyperbola fits in Supplemental Table S1 and show examples of the fitting process in Figure S2. Average permittivity and velocities are primarily estimated from hyperbola fits for 1961 basaltic lapilli at each of the three sites and for each frequency. Hyperbola measurements from the 1875 tephra were much more uncertain. These permittivities are elevated compared to typical values of 2-4 for a dry, low-density volcanic tephra deposit (Campbell and Ulrichs, 1969). Averages are summarized for the hyperbola fitting method in Table 2.

Table 2. Average permittivity and velocity from hypberbola fits for the three caldera sites.

Site	Tephra Cover	Frequency	Average Permittivity (ε_r')	Average Velocity (m/ns)
1	1961 Basaltic Tephra	200	13.9	0.080
1	1961 Basaltic Tephra	400	10.8	0.091
1	1961 Basaltic Tephra	900	7.5	0.109
2	1961 Basaltic Tephra	200	11.9	0.086
2	1961 Basaltic Tephra	400	10.2	0.094
2	1961 Basaltic Tephra	900	6.01	0.122
3	1875/1961 Tephras	200	18.3	0.071
3	1875/1961 Tephras	400	10.3	0.093
3	1961 Basaltic Tephra	400	15.2	0.079

Permittivity values estimated from trench and borehole measurements of tephra thickness are summarized in Table S2. We summarize averages of permittivity and corresponding velocity at all frequencies for all of the sites by capping tephra deposit in Table 3.

Table 3. Summary of average permittivity and velocity for each tephra deposit derived from tranches and boreholes.

Tephra Cover	Frequency (MHz)	Average Permittivity (ε_r')	Average Velocity (m/ns)

1961 Basaltic Tephra	200	4.79	0.137
1961 Basaltic Tephra	400	5.07	0.133
1961 Basaltic Tephra	900	5.08	0.133
1875 Tephra	200	5.47	0.128
1875 Tephra	400	4.37	0.143

Permittivity estimated from hyperbola fitting is elevated compared to the trench values. The hyperbola fitting method depends greatly on user identification of a true hyperbolic form and manual fitting of that shape. It is also highly sensitive to the goodness-of-fit of that of the theoretical hyperbola apex and tails to the true form, if that hyperbola is, in fact, real in the collected subsurface data (Giannakis et al., 2022). In particular, conventional hyperbola-fitting carries significant error when subsurface media are truly inhomogeneous (Giannakis et al., 2021). Fits to a false hyperbolic form yield elevated, unrealistic permittivity values which may have been retained in our sample leading to overestimates. This can be problematic even for automated hyperbola picking efforts where false and missed fits were shown to occur at 20% and 28%, respectively by Mertens et al. (2016). Furthermore, these hyperbola-fitting techniques can yield bulk velocities with variance and errors in the range of ± 10% or more (Jol, 2008). These likely sources of error result in these elevated permittivity and bulk velocity estimates, which highlights the limitations of conventional hyperbola fitting. We therefore utilize permittivity estimates from trenches and boreholes where possible in our analysis of losses and our ice thickness estimates.

4.3 Calculated Losses to the Radar Signal

Based on our observations at each site, we assume a median permittivity of 9 for what are likely underlying basalt lava flows with some possible 1875 ash and/or tephra cover at Site 1 (Units C and D; Carey et al., 2010) and a value of 3 for a dry tephra to represent the 1875 ash and/or tephra underlying the ice layer along some traverses at Sites 2 and 3 (Campbell and Ulrichs, 1969) in order to perform a multilayer depth-correction prior to fitting. The permittivity assumption for Site 3 is likely an underestimate as we could not measure whether there was any water at the base of the ice layer or deeper below; any meltwater would contribute to a higher bulk permittivity. Section 3.4 summarizes the permittivity assumptions for the ice and capping tephra layers. SeeTable S3 for a summary of all layer permittivities used for fitting.

Loss rate estimates result from portions of the corrected average trace (Figure 5a-d, gray curves) that display an exponential decay with depth. In all cases, this portion of the curve was from the base of the ice table, or pumice layer in the case of the Vikrahraun lava flow, to the noise floor. The majority of the remaining sources of loss that are contributing to the estimated loss rates after the spreading correction are therefore below the ice table, or the less lossy pumice transitioning to the underlying 1961 Vikrahraun flow in the ice-free case. This is due to the fitting depth range of the corrected trace that spans from the sub-ice or sub-pumice layers to the noise floor. The overlying tephra and ice contribute to the total loss, but likely to a lesser degree. We summarize the results of the attenuation for several representative ice-rich and ice-free radargrams in Figure 5a-d at each of the antenna center frequencies. Average one-way losses are summarized for the various ice-rich and ice-free stratigraphy in Table 4.

Figure S3 shows the average traces used for fitting in Figure 5a-d. Table S3 summarizes individual loss rate calculations.

Table 4. Summary of average one-way attenuation for ice-rich caldera stratigraphy and the ice-free, 1875 pumice-mantled 1961 Vikrahraun lava flow.

Stratigraphy	Frequency (MHz)	Average One-Way Attenuation (dB/m)
1961 Basaltic Tephra/Ice	200	2.69
1961 Basaltic Tephra/Ice	400	3.08
1961 Basaltic Tephra/Ice	900	4.55
1875 Tephra/Ice	200	1.52
1875 Tephra/Ice	400	1.67
1875 Pumice/1961 Vikrahraun Lava Flow	200	2.77
1875 Pumice/1961 Vikrahraun Lava Flow	400	0.76

The one-way total loss rates are similar, even at ice-free sites such as the 1961 Vikrahraun lava flow. The finer-grained, remobilized 1875 pumice that has mantled this basalt lava flow is likely the source of the comparable loss rates at this site (see Figure 1d). There is some overlap between all calculated loss rates at 200 MHz and 400 MHz in Figure 4e due to the spread in the values, likely the result of variability in scattering losses, meltwater, or properties of the material beneath the ice between the different sites. Despite this overlap, there is an overall increase in one-way loss with increasing frequency as observed by other investigations in permafrost environments (e.g., Boisson et al., 2011).

We estimate fitting errors by examining the variance in the slope fit over the same depth range to subsets of ten averaged traces at a time within the range of traces averaged for fitting. From this variance, we estimate standard deviation for the one-way loss rates derived from the slopes of the fit, which are shown as error bars in Figure 5e.These are summarized in Table S3. Larger ranges in standard deviation result from poor fits and deviations from a semilogarithmic decay for each of the ten traces sampled. There was no obvious correlation between the total number of traces and variance indicating higher variances are result from variations in goodness-of-fit from each of the ten trace samples. We found that the variance and standard deviation tend to increase with increasing frequency.The total number of loss rate estimates we were able to obtain was most often limited by a positive slope or low linear correlation coefficient, indicating a deviation from a semilogarithmic decay with depth. As a result, we obtained a limited number of loss estimates from Site 2 and radargrams with 1875 tephra burying ice (Site 3).

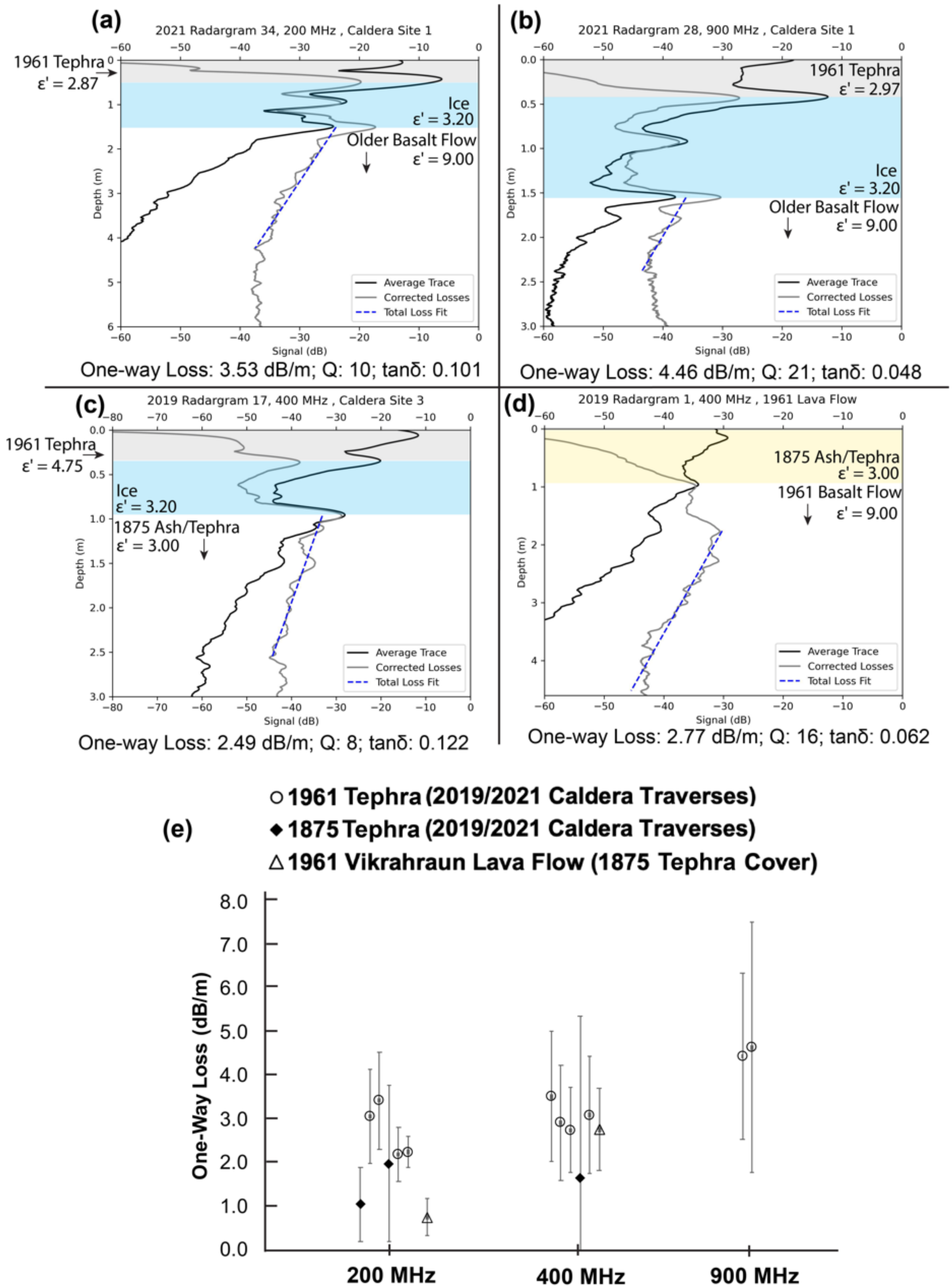
(a)
2021 Radargram 34, 200 MHz , Caldera Site 1
1961 Tephra
ε' = 2.87
Ice
ε' = 3.20
Older Basalt Flow
ε' = 9.00
Depth (m)
Signal (dB)
Average Trace
Corrected Losses
Total Loss Fit
One-way Loss: 3.53 dB/m; Q: 10; tanδ: 0.101
(b)
2021 Radargram 28, 900 MHz , Caldera Site 1
1961 Tephra
ε' = 2.97
Ice
ε' = 3.20
Older Basalt Flow
ε' = 9.00
Depth (m)
Signal (dB)
Average Trace
Corrected Losses
Total Loss Fit
One-way Loss: 4.46 dB/m; Q: 21; tanδ: 0.048
(c)
2019 Radargram 17, 400 MHz , Caldera Site 3
1961 Tephra
ε' = 4.75
Ice
ε' = 3.20
1875 Ash/Tephra
ε' = 3.00
Depth (m)
Signal (dB)
Average Trace
Corrected Losses
Total Loss Fit
One-way Loss: 2.49 dB/m; Q: 8; tanδ: 0.122
(d)
2019 Radargram 1, 400 MHz , 1961 Lava Flow
1875 Ash/Tephra
ε' = 3.00
1961 Basalt Flow
ε' = 9.00
Depth (m)
Signal (dB)
Average Trace
Corrected Losses
Total Loss Fit
One-way Loss: 2.77 dB/m; Q: 16; tanδ: 0.062
(e)
○ 1961 Tephra (2019/2021 Caldera Traverses)
◆ 1875 Tephra (2019/2021 Caldera Traverses)
△ 1961 Vikrahraun Lava Flow (1875 Tephra Cover)
One-Way Loss (dB/m)
200 MHz
400 MHz
900 MHz

Figure 5. We fit sections of semilogarithmic decay of trace averages at various sites and frequencies across the Askja caldera **(a-c)** and from the 1961 Vikrahraun basalt lava flow mantled with 1875 pumice **(d)**. Figure S3 shows the traces averaged in this figure on their respective radargrams. The average trace (solid black line) is corrected for geometric spreading effects (gray solid line). Sections of semilogarithmic decay with depth are fit with a linear regression (blue dashed line). Losses are comparable between the Site 3 and 1961 Lava Flow observations at the same frequency (Panels c and d). Thicknesses of the shaded regions correspond to the estimated thickness of the deposit for those averaged traces. Thicknesses of the deposit(s) underlying the ice is unknown in all cases. One-way loss in dB/m calculated from the slope of the fit (blue-dashed line), Q, and the loss tangent (tan δ) are shown. **(e)** One-way attenuation at 200, 400, and 900 MHz increases with increasing frequency. Points at each center frequency are spread out for clarity. There is significant spread in the losses associated with each deposit at each frequency. We report slopes of successful fits along with other parameters in Table S3.

5 Discussion

5.1 Bulk Radar Losses as an Indicator of Buried Ice

We tested whether total radar attenuation can be used as a diagnostic signature of buried ice to address ambiguity that arises when interpreting radar data collected over stratigraphy sharing similar or overlapping dielectric properties. Askja was chosen for its substantial massive ice reservoirs buried by the dry, low-density, unconsolidated volcanic ash and tephra that directly overlaps in permittivity with that of water ice (Campbell and Ulrichs, 1969; Johari et al., 1976; Matsuoka et al., 1997). Pure ice typically exhibits a lower loss than other geologic materials at microwave frequencies (Daniels, 2004; Pettinelli et al., 2015). The meters of ice in the caldera coupled with the tephra as a geophysical stand-in for regolith cover generated the best case scenario to test whether total attenuation yields a diagnostic signature of ice-rich versus ice-free stratigraphy.

Measured loss rates between ice-rich sites and the ice-free comparison site share much overlap in magnitude (Figure 5e), especially considering their associated formal errors (see

Table S3). This makes it challenging to uniquely identify the characteristic low-loss signature of subsurface ice at these field sites by evaluating of trends in loss rates versus frequency (see Figure S4 for comparison to literature values). However, some of this ambiguity may be the result of the limited ice thicknesses encountered at our field locations and contributions of deeper volcanic materials to the measured loss rates. As discussed in Section 4.3, to achieve a reliable slope measurement, our one-way loss estimates require fits to the average trace over depth ranges that fall below the ice layer in all cases. Depending on the ice layer thickness, the combined loss of the tephra overburden and volcanic material that is below the ice (e.g., lava flows or older tephra layers) may contribute more greatly to the loss. Indeed, we find that one-way losses decrease with increasing average ice thickness across all frequencies (Figure 6), suggesting that the signature of ice is likely to be more prominently expressed and identified as greater thicknesses are encountered.

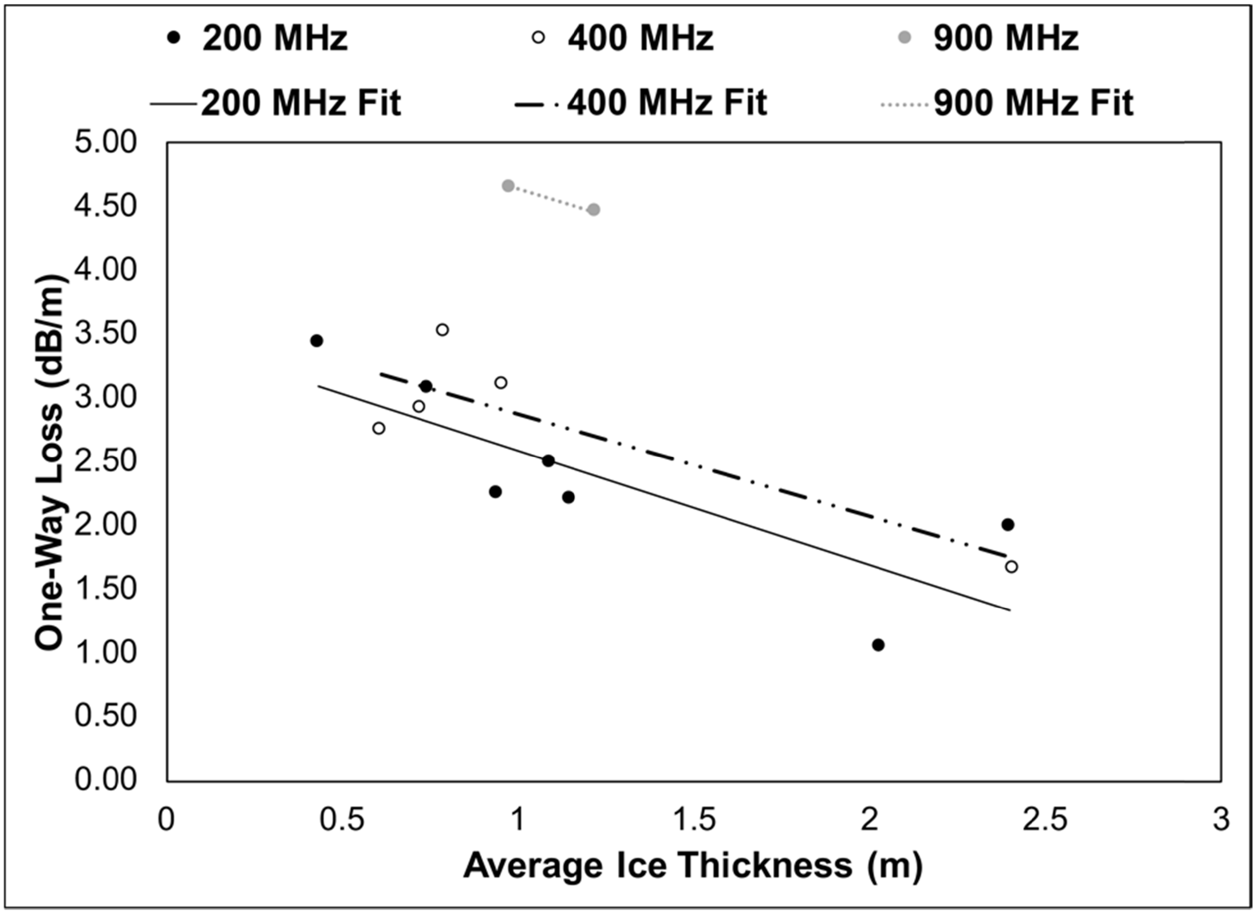

Figure 6. One-way losses decrease with increasing average ice thickness along sections of GPR traverses comprising the average trace at each site. This trend is likely biased by the higher number of loss rate fits obtained at 200 MHz. The trendline for the 200 MHz is the solid black line; the trends for other frequencies are dashed lines.

Additional data points are needed to fully evaluate the relationship between one-way losses and average ice thicknesses. While all frequencies demonstrate this behavior, the 200 MHz data show a stronger correlation. The trends in Figure 6 are biased by the higher total number of loss rate fits that were able to be obtained at 200 MHz.

5.2 Other Sources of Loss

The total losses we estimated are comprised of contributions from both absorption and scattering. Without a full characterization these effects, it is difficult to determine if losses are simply driven by the different scattering regimes created by the various tephra clast sizes (mm-scale 1961 lapilli vs. cm-scale 1875 pumice) and material below the ice layer (such as lava flows or older tephra), or absorption, or a combination of both. In Figure 5, for example, the larger cm-to-dm-scale 1875 pumice clasts overlying massive ice exhibit a lower loss at 200 MHz than the observations over the 1961 lapilli at the same frequency. We observed that scattering became more visually prevalent in the 400 and 900 MHz radargrams in the 1875 pumice deposit, suggesting that scattering is dominant at these frequencies and to a lesser extent at 200 MHz. In the 1961 basaltic tephra deposit, absorption may be more dominant at 200 MHz given the sub-wavelength clast sizes (lapilli) associated with that deposit. Additionally, traverses with 1875 pumice coverage have thicker ice layers on average. Given the correlation between lower loss rates and average ice thickness (Figure 6), the lower loss rates observed for the 1875 pumice traverses could be the result of a thicker ice layer at depth for those traces. This highlights the need for further modeling and independent measurments of contributions from absorption in order to fully characterize and isolate the individual contributions to total attenuation.

5.3 Insights on GPR Deployment from the Askja Analog Site

Askja presents a testbed to conduct controlled geophysical experiments for future operations, instrument deployment, and post-collection analyses that can be used to identify resources of interest for real-time decision-making during surface missions. The unvegetated terrain within the caldera and surrounding regions share a striking similarity to the surfaces of the Moon and Mars. Unsurprisingly, the ambiguity associated with GPR returns from the subsurface there necessitated additional context such as boreholes or trenching in order to confirm our interpretation of stratigraphy. This will no doubt be a challenge on the surfaces of other terrestrial bodies for both robotic and human assets. Here we discuss lessons learned from Askja and implications for GPR field deployment and analysis of radar attenuation for future ISRU analog investigations and more broadly, cryogeophysics in volcanic terrains.

The frequency range used to map the tephra and ice in the caldera was successful at resolving the entire vertical extent of both the tephra and massive ice, where present, at all sites. All three center frequencies performed exceptionally well when taking data over the mm-sized 1961 basaltic lapilli. 200 MHz was particularly advantageous for overcoming the effects of scattering from the cm-to-dm-sized clasts of 1875 pumice, especially at Site 3. 400 MHz provided a better balance of vertical resolution and penetration depth, particularly at Sites 1 and 2. Surveying at the 900 MHz center frequency was challenging at all sites except for Site 1 where a combination of conditions including smoother, more compact tephra (enabling constant ground coupling) and small clast sizes allowed for collection of high-quality radargrams. The finer vertical resolution at this frequency also enabled greatly improved identification of bedding and internal layering in the tephra. For any resource campaigns conducted on the surface of the Moon or Mars where higher amounts of scattering in the regolith may be a concern, lower frequencies will likely be more favorable, unless the characterization of very-near surface ice is desired, such as what was encountered at the high latitudes of Mars by the Phoenix Lander (Mellon et al., 2009).

Our GPR surveys across the three caldera floor sites did not resolve vertical transitions between pore ice and massive ice. Our trench and borehole observations showed thin (generally <10 cm) zones of pore-ice within the tephra before transitioning to massive ice at depth. These zones in pore ice and transitions in ice concentration are at or below the limit of vertical resolution for the GPR frequencies used here, making them difficult to identify in radargrams. To test GPR's ability to characterize changes in ice concentration for future planetary science and ISRU applications, more suitable analog sites should be sought. This will be important for future interpretation of Mars ground data and especially for the Moon, since ice in the form of pore-filling zones or small grain sizes may be most prevalent, at least in the near-surface (Siegler et al., 2015).

The Askja caldera tephra deposits are not precisely compositionally analogous to lunar or martian regolith but are of a similar density and permittivity when dry (see Carrier et al., 1991; Olhoeft and Strangway, 1975; Lai et al., 2019). Meltwater and moisture, although relatively minimal at Askja at the time of observations, will be an issue for GPR investigations at any Earth analog site. This thin zone of perched meltwater at the top of the ice layer likely enhanced the dielectric contrast between the ice and overlying tephra, which are otherwise close or overlap in permittivity (e.g., Campbell and Ulrichs, 1969; Boisson et al., 2011). Although the effects of this meltwater on the attenuation are likely minimal, water may substantially contribute to the total loss, which could explain the lower loss rates estimated for the 1875 pumice-mantled Vikrahraun lava flow. Characterization of moisture at any analog site is necessary in order to isolate its contributions to radar attenuation. In order to directly compare results from future terrestrial analog field GPR investigations with the arid martian or lunar environments, soil moisture probe measurements with depth or coordinated electrical resistivity measurements to quantify contributions to the total attenuation from meltwater or moisture should be included in the field plan. Effects of moisture may be further minimized by field studies in extreme regions such as the high Andes or the Antarctic Dry Valleys. Despite these shortfalls and complexities, the Askja caldera deposits offer variation in clast sizes, intra-grain and intergrain porosities, varying ice thicknesses, and ice burial by a low-density overburden. This diversity makes Askja not only an ideal testbed for ISRU applications, but also an important site for studying volcano-ice interaction and Icelandic permafrost reservoirs.

6 Conclusions

We conducted the first ground-penetrating radar survey of tephra sourced from the eruptions of Askja in 1875 and 1961 that buried and preserved layers of massive ice. The overlapping dielectric properties of the Askja tephra deposits and meters-thick massive ice layers make this site an ideal location to test GPR data analysis techniques for future *in-situ* resource utilization objectives for the Moon and Mars. Determining detection thresholds for water ice deposit thicknesses and concentrations is important for future interpretation of GPR observations at the Moon and Mars where concentrations are expected to be lower and ice-regolith mixtures could produce a nonunique signature. We estimated and compared total attenuation rates between ice-rich and ice-free stratigraphy to determine if massive ice at depth produces a diagnostic loss signature at multiple ground-penetrating radar center frequencies.

GPR successfully delineated the vertical and horizontal extent of shallow ice deposits at Askja. Loss rates across all frequencies and at all sites with different tephra cover and ice thicknesses were characteristically low. Loss rates increase with increasing frequency and decrease with increasing ice thickness.Thicker layers of ice that comprise a larger fraction of the overall attenuation path length of the radar signal may yield improved detectability using this method. While attenuation may not be solely diagnostic of the signature of water ice, when combined with analyses of reflectors and hyperbola fitting, a non-unique result can be obtained. Pore ice, ice and regolith mixtures, and generally low concentrations of ice will be challenging to uniquely identify using traditional approaches to GPR data analysis. More data points at additional frequencies would provide more confidence in these trends. Additional modeling and measurements of contributions to the total attenuation from scattering and absorption will be necessary to further isolate the signature of massive ice.

Acknowledgments

This work was supported NASA's Planetary Science Division Research Program, through the Goddard Instrument Field Team as a part of the 2019/2021 Volcanic Deposit Evolution and Origins (VIDEO) expeditions. PLW was supported by NASA under award number #80GSFC21M0002. Contributions by JAR were supported by the NASA SSERVI GEODES grant #80NSSC19M0216. We thank the Vatnajökull National Park in Iceland for their support and permission to carry out this work. The authors thank Nicole Whelley and Caela Barry for providing logistical support for the safe and productive VIDEO expeditions. The authors also thank the two anonymous reviewers whose insightful comments greatly improved this manuscript.

Open Research

Ground-penetrating radar and UAS data used in this paper can be accessed via the USGS ScienceBase data repository (doi and citation TBD). **Archiving is currently underway and pending USGS review. A temporary link to access these data for review is: https://www.sciencebase.gov/catalog/item/6419fd7dd34eb496d1d2a141/tokenEntry/1be3e3e7-158a-44bf-88ae-df223edfac3f-18b00ad1893T.** Landsat-8 imagery are publicly available for download from the USGS EarthExplorer (https://doi.org/10.5066/P9OGBGM6). The Radar

Analysis Graphical Utility (Tober and Christoffersen, 2020) used in our investigation is available for download at https://github.com/btobers/RAGU. The readgssi software (Nesbitt et al., 2022) is available for download at https://github.com/iannesbitt/readgssi. The code developed by Shoemaker (2023) is available for download at https://github.com/emileighshoemaker/Askja-Radar-Loss.

References

Annan, A. P., & Davis, J. L. (1977). Radar range analysis for geological materials. *Geological Survey of Canada*, *77*(1B), 117-124.

Annertz, K., Nilsson, M., & Sigvaldason, G. E. (1985). *The postglacial history of Dyngjufjöll*. Nordic volcanological Institute, University of Iceland.

Blasizzo, A. Y., Ukstins, I. A., Scheidt, S. P., Graettinger, A. H., Peate, D. W., Carley, T. L., Moritz, A. J., & Thines, J. E. (2022). Vikrahraun—the 1961 basaltic lava flow eruption at Askja, Iceland: Morphology, geochemistry, and planetary analogs. *Earth, Planets and Space*, *74*(1), 168. https://doi.org/10.1186/s40623-022-01711-5

Boisson, J., Heggy, E., Clifford, S. M., Yoshikawa, K., Anglade, A., & Lognonné, P. (2011). Radar sounding of temperate permafrost in Alaska: Analogy to the Martian midlatitude to high-latitude ice-rich terrains. *Journal of Geophysical Research: Planets*, *116*(E11). https://doi.org/10.1029/2010JE003768

Bramson, A. M., Byrne, S., Putzig, N. E., Sutton, S., Plaut, J. J., Brothers, T. C., & Holt, J. W. (2015). Widespread excess ice in Arcadia Planitia, Mars. *Geophysical Research Letters*, *42*(16), 6566–6574. https://doi.org/10.1002/2015GL064844

Brandt, O., Langley, K., Kohler, J., & Hamran, S.-E. (2007). Detection of buried ice and sediment layers in permafrost using multi-frequency Ground Penetrating Radar: A case examination on Svalbard. *Remote Sensing of Environment*, *111*(2), 212–227. https://doi.org/10.1016/j.rse.2007.03.025

Campbell, M. J., & Ulrichs, J. (1969). Electrical properties of rocks and their significance for lunar radar observations. *Journal of Geophysical Research (1896-1977)*, *74*(25), 5867–5881. https://doi.org/10.1029/JB074i025p05867

Campbell, S., Affleck, R. T., & Sinclair, S. (2018). Ground-penetrating radar studies of permafrost, periglacial, and near-surface geology at McMurdo Station, Antarctica. *Cold Regions Science and Technology*, *148*, 38–49. https://doi.org/10.1016/j.coldregions.2017.12.008

Cannon, K. M., & Britt, D. T. (2020). A geologic model for lunar ice deposits at mining scales. *Icarus*, *347*, 113778. https://doi.org/10.1016/j.icarus.2020.113778

Carey, R. J., Houghton, B. F., & Thordarson, T. (2008a). Contrasting styles of welding observed in the proximal Askja 1875 eruption deposits I: Regional welding. *Journal of Volcanology and Geothermal Research*, *171*(1), 1–19. https://doi.org/10.1016/j.jvolgeores.2007.11.020

Carey, R. J., Houghton, B. F., & Thordarson, T. (2008b). Contrasting styles of welding observed in the proximal Askja 1875 eruption deposits II: Local welding. *Journal of Volcanology and Geothermal Research*, *171*(1), 20–44. https://doi.org/10.1016/j.jvolgeores.2007.11.017

Carey, R. J., Houghton, B. F., & Thordarson, T. (2009). Abrupt shifts between wet and dry phases of the 1875 eruption of Askja Volcano: Microscopic evidence for macroscopic dynamics. *Journal of Volcanology and Geothermal Research*, *184*(3), 256–270. https://doi.org/10.1016/j.jvolgeores.2009.04.003

Carey, R. J., Houghton, B. F., & Thordarson, T. (2010). Tephra dispersal and eruption dynamics of wet and dry phases of the 1875 eruption of Askja Volcano, Iceland. *Bulletin of Volcanology*, *72*(3), 259–278. https://doi.org/10.1007/s00445-009-0317-3

Carrier, W. D., III, Olhoeft, G. R., & Mendell, W. (1991). Physical Properties of the Lunar Surface. In *Lunar Sourcebook, A User's Guide to the Moon* (pp. 475–594). https://ui.adsabs.harvard.edu/abs/1991lsug.book..475C

Colaprete, A. (2021). *Volatiles Investigating Polar Exploration Rover (VIPER)*. https://ntrs.nasa.gov/citations/20210015009

Czekirda, J., Westermann, S., Etzelmüller, B., & Jóhannesson, T. (2019). Transient Modelling of Permafrost Distribution in Iceland. *Frontiers in Earth Science*, *7*, 130. https://doi.org/10.3389/feart.2019.00130

Daniels, D. J. (Ed.). (2004). *Ground Penetrating Radar*. (Vol. 1). IET.

Dinwiddie, C. L., Clifford, S. M., Grimm, R. E., & Heggy, E. (2005). *Strategy for Selection of Mars Geophysical Analogue Sites*. 29.

Dundas, C. M., Bramson, A. M., Ojha, L., Wray, J. J., Mellon, M. T., Byrne, S., McEwen, A. S., Putzig, N. E., Viola, D., Sutton, S., Clark, E., & Holt, J. W. (2018). Exposed subsurface ice sheets in the Martian mid-latitudes. *Science*, *359*(6372), 199–201. https://doi.org/10.1126/science.aao1619

Ellery, A. (2020). Sustainable in-situ resource utilization on the moon. *Planetary and Space Science*, *184*, 104870. https://doi.org/10.1016/j.pss.2020.104870

Etzelmüller, B., Farbrot, H., Guðmundsson, Á., Humlum, O., Tveito, O. E., & Björnsson, H. (2007). The regional distribution of mountain permafrost in Iceland. *Permafrost and Periglacial Processes*, *18*(2), 185–199. https://doi.org/10.1002/ppp.583

Etzelmüller, B., Patton, H., Schomacker, A., Czekirda, J., Girod, L., Hubbard, A., Lilleøren, K. S., & Westermann, S. (2020). Icelandic permafrost dynamics since the Last Glacial Maximum – model results and geomorphological implications. *Quaternary Science Reviews*, *233*, 106236. https://doi.org/10.1016/j.quascirev.2020.106236

Fang, G.-Y., Zhou, B., Ji, Y.-C., Zhang, Q.-Y., Shen, S.-X., Li, Y.-X., Guan, H.-F., Tang, C.-J., Gao, Y.-Z., Lu, W., Ye, S.-B., Han, H.-D., Zheng, J., & Wang, S.-Z. (2014). Lunar Penetrating Radar onboard the Chang'e-3 mission. *Research in Astronomy and Astrophysics*, *14*(12), 1607–1622. https://doi.org/10.1088/1674-4527/14/12/009

Farrokhi, M., Hamzehloo, H., Rahimi, H., & Allameh Zadeh, M. (2016). Separation of intrinsic and scattering attenuation in the crust of central and eastern Alborz region, Iran. *Physics of the Earth and Planetary Interiors*, *253*, 88–96. https://doi.org/10.1016/j.pepi.2016.02.005

Giannakis, I., Zhou, F., Warren, C., & Giannopoulos, A. (2022). On the Limitations of Hyperbola Fitting for Estimating the Radius of Cylindrical Targets in Nondestructive Testing and Utility Detection. *IEEE Geoscience and Remote Sensing Letters*, *19*, 1–5. https://doi.org/10.1109/LGRS.2022.3195947

Giannakis, I., Zhou, F., Warren, C., & Giannopoulos, A. (2021). Inferring the Shallow Layered Structure at the Chang'E-4 Landing Site: A Novel Interpretation Approach Using Lunar Penetrating Radar. *Geophysical Research Letters*, *48*(16), e2021GL092866. https://doi.org/10.1029/2021GL092866

Graettinger, A. H., Ellis, M. K., Skilling, I. P., Reath, K., Ramsey, M. S., Lee, R. J., Hughes, C. G., & McGarvie, D. W. (2013). Remote sensing and geologic mapping of glaciovolcanic deposits in the region surrounding Askja (Dyngjufjöll) volcano, Iceland. *International Journal of Remote Sensing*, *34*(20), 7178–7198. https://doi.org/10.1080/01431161.2013.817716

Grimm, R. E., Heggy, E., Clifford, S., Dinwiddie, C., McGinnis, R., & Farrell, D. (2006). Absorption and scattering in ground-penetrating radar: Analysis of the Bishop Tuff. *Journal of Geophysical Research: Planets*, *111*(E6). https://doi.org/10.1029/2005JE002619

Hamran, S.-E., Paige, D. A., Allwood, A., Amundsen, H. E. F., Berger, T., Brovoll, S., Carter, L., Casademont, T. M., Damsgård, L., Dypvik, H., Eide, S., Fairén, A. G., Ghent, R., Kohler, J., Mellon, M. T., Nunes, D. C., Plettemeier, D., Russell, P., Siegler, M., & Øyan, M. J. (2022). Ground penetrating radar observations of subsurface structures in the floor of Jezero crater, Mars. *Science Advances*, *8*(34), eabp8564. https://doi.org/10.1126/sciadv.abp8564

Hamran, S.-E., Paige, D. A., Amundsen, H. E. F., Berger, T., Brovoll, S., Carter, L., Damsgård, L., Dypvik, H., Eide, J., Eide, S., Ghent, R., Helleren, Ø., Kohler, J., Mellon, M., Nunes, D. C., Plettemeier, D., Rowe, K., Russell, P., & Øyan, M. J. (2020). Radar Imager for Mars' Subsurface

Experiment—RIMFAX. *Space Science Reviews*, *216*(8), 128. https://doi.org/10.1007/s11214-020-00740-4

Hartley, M. E., Thordarson, T., & de Joux, A. (2016). Postglacial eruptive history of the Askja region, North Iceland. *Bulletin of Volcanology*, *78*(4), 28. https://doi.org/10.1007/s00445-016-1022-7

Heggy, E., Clifford, S. M., Grimm, R. E., Dinwiddie, C. L., Stamatakos, J. A., & Gonzalez, S. H. (2006). Low-frequency radar sounding investigations of the North Amargosa Desert, Nevada: A potential analog of conductive subsurface environments on Mars. *Journal of Geophysical Research: Planets*, *111*(E6). https://doi.org/10.1029/2005JE002523

Heggy, E., Clifford, S. M., Grimm, R. E., Dinwiddie, C. L., Wyrick, D. Y., & Hill, B. E. (2006). Ground-penetrating radar sounding in mafic lava flows: Assessing attenuation and scattering losses in Mars-analog volcanic terrains. *Journal of Geophysical Research: Planets*, *111*(E6). https://doi.org/10.1029/2005JE002589

Helgason, J. (2000, May). Ground ice in iceland: possible analogs for equatorial Mars. In *Second International Conference on Mars Polar Science and Exploration* (No. 1057, p. 72).

Holt, J. W., Safaeinili, A., Plaut, J. J., Head, J. W., Phillips, R. J., Seu, R., Kempf, S. D., Choudhary, P., Young, D. A., Putzig, N. E., Biccari, D., & Gim, Y. (2008). Radar Sounding Evidence for Buried Glaciers in the Southern Mid-Latitudes of Mars. *Science*, *322*(5905), 1235–1238. https://doi.org/10.1126/science.1164246

Jin, A., Mayeda, K., Adams, D., & Aki, K. (1994). Separation of intrinsic and scattering attenuation in southern California using TERRAscope data. *Journal of Geophysical Research: Solid Earth*, *99*(B9), 17835–17848. https://doi.org/10.1029/94JB01468

Johari, G. P. (1976). The dielectric properties of H2O and D2O ice Ih at MHz frequencies. *The Journal of Chemical Physics*, *64*(10), 3998–4005. https://doi.org/10.1063/1.432033

Jol, H. M. (Ed.). (2008). *Ground penetrating radar theory and applications*. Elsevier.

Kellerer-Pirklbauer, A., Farbrot, H., & Etzelmüller, B. (2007). Permafrost aggradation caused by tephra accumulation over snow-covered surfaces: Examples from the Hekla-2000 eruption in Iceland. *Permafrost and Periglacial Processes*, *18*(3), 269–284. https://doi.org/10.1002/ppp.596

Lai, J., Xu, Y., Zhang, X., Xiao, L., Yan, Q., Meng, X., Zhou, B., Dong, Z., & Zhao, D. (2019). Comparison of Dielectric Properties and Structure of Lunar Regolith at Chang'e-3 and Chang'e-4 Landing Sites Revealed by Ground-Penetrating Radar. *Geophysical Research Letters*, *46*(22), 12783–12793. https://doi.org/10.1029/2019GL084458

Li, C., Su, Y., Pettinelli, E., Xing, S., Ding, C., Liu, J., Ren, X., Lauro, S. E., Soldovieri, F., Zeng, X., Gao, X., Chen, W., Dai, S., Liu, D., Zhang, G., Zuo, W., Wen, W., Zhang, Z., Zhang, X., & Zhang, H. (2020). The Moon's farside shallow subsurface structure unveiled by Chang'E-

4 Lunar Penetrating Radar. *Science Advances*, *6*(9), eaay6898. https://doi.org/10.1126/sciadv.aay6898

Li, C., Zheng, Y., Wang, X., Zhang, J., Wang, Y., Chen, L., Zhang, L., Zhao, P., Liu, Y., Lv, W., Liu, Y., Zhao, X., Hao, J., Sun, W., Liu, X., Jia, B., Li, J., Lan, H., Fa, W., … Wu, F. (2022). Layered subsurface in Utopia Basin of Mars revealed by Zhurong rover radar. *Nature*, 1–5. https://doi.org/10.1038/s41586-022-05147-5

LWIMS Report (2020) Lunar Water ISRU Measurement Study (LWIMS): Establishing a Measurement Plan for Identification and Characterization of a Water Reserve https://ntrs.nasa.gov/citations/20205008626

Matsuoka, T., Fujita, S., & Mae, S. (1997). Dielectric Properties of Ice Containing Ionic Impurities at Microwave Frequencies. *The Journal of Physical Chemistry B*, *101*(32), 6219–6222. https://doi.org/10.1021/jp9631590

Mellon, M. T., Arvidson, R. E., Sizemore, H. G., Searls, M. L., Blaney, D. L., Cull, S., Hecht, M. H., Heet, T. L., Keller, H. U., Lemmon, M. T., Markiewicz, W. J., Ming, D. W., Morris, R. V., Pike, W. T., & Zent, A. P. (2009). Ground ice at the Phoenix Landing Site: Stability state and origin. *Journal of Geophysical Research: Planets*, *114*(E1). https://doi.org/10.1029/2009JE003417

MEPAG ICE-SAG Final Report (2019), Report from the Ice and Climate Evolution Science Analysis group (ICE-SAG), Chaired by S. Diniega and N. E. Putzig, 157 pages posted 08 July 2019, by the Mars Exploration Program Analysis Group (MEPAG) at http://mepag.nasa.gov/reports.cfm.

Mertens, L., Persico, R., Matera, L., & Lambot, S. (2016). Automated Detection of Reflection Hyperbolas in Complex GPR Images With No A Priori Knowledge on the Medium. *IEEE Transactions on Geoscience and Remote Sensing*, *54*(1), 580–596. https://doi.org/10.1109/TGRS.2015.2462727

Morgan, G. A., Putzig, N. E., Perry, M. R., Sizemore, H. G., Bramson, A. M., Petersen, E. I., Bain, Z. M., Baker, D. M. H., Mastrogiuseppe, M., Hoover, R. H., Smith, I. B., Pathare, A., Dundas, C. M., & Campbell, B. A. (2021). Availability of subsurface water-ice resources in the northern mid-latitudes of Mars. *Nature Astronomy*, *5*(3), Article 3. https://doi.org/10.1038/s41550-020-01290-z

Nesbitt, I., Simon, F.-X., Hoffmann, F., Paulin, T., Shaw, T. (2022). readgssi: an Open-Source Tool to Read and Plot GSSI Ground-Penetrating Radar Data (0.0.21). Zenodo. https://doi.org/10.5281/zenodo.5932420 [Software]

Olhoeft, G. R., & Strangway, D. W. (1975). Dielectric properties of the first 100 meters of the Moon. *Earth and Planetary Science Letters*, *24*(3), 394–404. https://doi.org/10.1016/0012-821X(75)90146-6

Pettinelli, E., Cosciotti, B., Di Paolo, F., Lauro, S. E., Mattei, E., Orosei, R., & Vannaroni, G. (2015). Dielectric properties of Jovian satellite ice analogs for subsurface radar exploration: A review. *Reviews of Geophysics*, *53*(3), 593–641. https://doi.org/10.1002/2014RG000463

Picardi, G., Biccari, D., Seu, R., Marinangeli, L., Johnson, W. T. K., Jordan, R. L., Plaut, J., Safaenili, A., Gurnett, D. A., Ori, G. G., Orosei, R., Calabrese, D., & Zampolini, E. (2004). Performance and surface scattering models for the Mars Advanced Radar for Subsurface and Ionosphere Sounding (MARSIS). *Planetary and Space Science*, *52*(1), 149–156. https://doi.org/10.1016/j.pss.2003.08.020

Richardson, J. A., Esmaeili, S., Baker, D. M. H., Shoemaker, E. S., Kruse, S., Jazayeri, S., Whelley, P. L., Garry, W. B., Bell, E., Young, K. E., Carter, L. M., Schmerr, N. (2020). Prospecting Buried Resources with Ground Penetrating Radar. *Lunar Surface Science Workshop 2020* (No. 5134)

Scabbia, G., & Heggy, E. (2018). Quantifying Subsurface Propagation Losses for VHF Radar Sounding Waves in Hyper-Arid Terrains. *IGARSS 2018 - 2018 IEEE International Geoscience and Remote Sensing Symposium*, 6800–6803. https://doi.org/10.1109/IGARSS.2018.8517891

Seu, R., Phillips, R. J., Biccari, D., Orosei, R., Masdea, A., Picardi, G., Safaeinili, A., Campbell, B. A., Plaut, J. J., Marinangeli, L., Smrekar, S. E., & Nunes, D. C. (2007). SHARAD sounding radar on the Mars Reconnaissance Orbiter. *Journal of Geophysical Research: Planets*, *112*(E5). https://doi.org/10.1029/2006JE002745

Shoemaker, E. S., Baker, D. M. H., Richardson, J. A., Carter, L. M., Young, K. E., Whelley, P. L., Schmerr, N., Wike, L., Coonan, J., Kruse, S. (2022). Ground-Penetrating Radar as a Tool for Prospecting Buried Lunar Ice. *Lunar Surface Science Workshop 17* (No. 5045)

Shoemaker E. S. (2023). Askja Radar Loss: Radar Loss Initial Release (v1.0.0). Zenodo. https://doi.org/10.5281/zenodo.7562601 [Software]

Siegler, M., Paige, D., Williams, J.-P., & Bills, B. (2015). Evolution of lunar polar ice stability. *Icarus*, *255*, 78–87. https://doi.org/10.1016/j.icarus.2014.09.037

Skolnik, M. I. (2008). *Radar handbook*. McGraw-Hill Education.

Sparks, R. S. J., Wilson, L., Sigurdsson, H., & Walker, G. P. L. (1981). The pyroclastic deposits of the 1875 eruption of Askja, Iceland. *Philosophical Transactions of the Royal Society of London. Series A, Mathematical and Physical Sciences*, *299*(1447), 241–273. https://doi.org/10.1098/rsta.1981.0023

Starr, S. O., & Muscatello, A. C. (2020). Mars in situ resource utilization: A review. *Planetary and Space Science*, *182*, 104824. https://doi.org/10.1016/j.pss.2019.104824

Stuurman, C. M., Osinski, G. R., Holt, J. W., Levy, J. S., Brothers, T. C., Kerrigan, M., & Campbell, B. A. (2016). SHARAD detection and characterization of subsurface water ice deposits in Utopia Planitia, Mars. *Geophysical Research Letters*, *43*(18), 9484–9491. https://doi.org/10.1002/2016GL070138

Thorarinsson, S., & Sigvaldason, G. E. (1962). The eruption in Askja, 1961; a preliminary report. *American Journal of Science*, *260*(9), 641–651. https://doi.org/10.2475/ajs.260.9.641

Tober, B. S., & Christoffersen, M. S. (2020). Radar Analysis Graphical Utility. Zenodo. https://doi.org/10.5281/zenodo.4437841 [Software]

Vermote, E., Justice, C., Claverie, M., & Franch, B. (2016). Preliminary analysis of the performance of the Landsat 8/OLI land surface reflectance product. *Remote Sensing of Environment*, *185*, 46–56. https://doi.org/10.1016/j.rse.2016.04.008